

# Properties of spherical galaxies and clusters with an NFW density profile

Ewa L. Łokas<sup>1</sup> and Gary A. Mamon<sup>2,3</sup>

<sup>1</sup>*Copernicus Astronomical Center, Bartycka 18, 00–716 Warsaw, Poland*

<sup>2</sup>*Institut d’Astrophysique de Paris (CNRS UPR 341), 98 bis Bd Arago, F–75014 Paris, France*

<sup>3</sup>*DAEC (CNRS UMR 8631), Observatoire de Paris, Place Jules Janssen, F–92195 Meudon, France*

2 December 2024

## ABSTRACT

Using the standard dynamical theory of spherical systems, we calculate the properties of spherical galaxies and clusters with isotropic velocity tensors whose density profiles obey the universal form first obtained in high resolution cosmological  $N$ -body simulations by Navarro, Frenk & White. Analytical solutions are found for the radial dependence of the mass, gravitational potential, velocity dispersion, energy and virial ratio and we test their variability with the concentration parameter describing the density profile. We also compute structural parameters, such as half-mass radius, effective radius and various measures of concentration. Finally, we derive projected quantities, the surface mass density and line-of-sight as well as aperture velocity dispersion, all of which can be directly applied in observational tests of current scenarios of structure formation.

On the mass scales of galaxies, if constant mass-to-light is assumed, the NFW surface density profile is found to fit well Hubble-Reynolds laws. It is also well fitted by Sérsic  $R^{1/m}$  laws, for  $m \simeq 3$ , but in a much narrower range of  $m$  and with much larger effective radii than are observed. Assuming in turn reasonable values of the effective radius, the mass density profiles imply a mass-to-light ratio that increases outwards at all radii. Hence, the NFW model seems inconsistent with the observations of elliptical galaxies.

**Key words:** methods: analytical – galaxies: clusters: general – large-scale structure of Universe

## 1 INTRODUCTION

A universal profile of dark matter haloes was introduced as a result of high-resolution  $N$ -body simulations performed by Navarro, Frenk & White (1995, 1996, 1997, hereafter NFW) for power-law as well as CDM initial power spectra of density fluctuations. NFW found that in a large range of masses the density profiles of dark haloes can be fitted with a simple formula with only one fitting parameter. The density profile steepens from  $r^{-1}$  near the centre of the halo to  $r^{-3}$  at large distances. The NFW profile has been confirmed in cosmological simulations by Cole & Lacey (1996), Tormen, Bouchet & White (1997), Huss, Jain & Steinmetz (1999a), Jing (1999), Bullock et al. (1999), while Huss, Jain & Steinmetz (1999b) have shown that the NFW profile also arises from non-cosmological initial conditions. It is worthwhile noting that some (but not all) recent very high resolution cosmological simulations produce steeper density profiles, with inner slopes  $\simeq -1.5$  (Fukushige & Makino 1997, Moore et al. 1998, Ghigna et al. 1999, see also Jing & Suto 2000). The density profiles in the cosmological simulations

also display considerable scatter (Avila-Reese et al. 1999, Bullock et al. 1999), and Avila-Reese et al. find that the outer slopes of galaxy size haloes are steeper than the NFW slope of  $-3$  when selected within clusters ( $-4$ ) and slightly shallower within groups ( $-2.7$ ). Although the exact properties of dark matter haloes are still under debate, the NFW profile is presently considered to provide the reference frame for any further numerical research on density profiles of dark haloes.

Simple cosmological derivations of the density profiles of bound objects are difficult, essentially because one needs to work in the non-linear regime of the growth of gravitational instabilities. Nevertheless, using the spherical *top-hat* model of Gunn & Gott (1972), density profiles typically varying as  $r^{-9/4}$  were derived by Gott (1975), Gunn (1977), Fillmore & Goldreich (1984) and Bertschinger (1985). Hoffman & Shaham (1985) applied the spherical infall model to the hierarchical clustering scenario and predicted that the density profiles of haloes should depend on  $\Omega$  as well as the initial power spectrum of density fluctuations. However, for  $\Omega = 1$

they obtained power-law profiles in contradiction with the steepening slopes found in the current  $N$ -body simulations described above. In a recent study, Lokas (2000, see also Lokas 1999a, 1999b) has improved the model of Hoffman & Shaham (1985) by a generalization of the initial density distribution, the introduction of a cut-off in this distribution at half the inter-peak separation and by a proper calculation of the collapse factor. The improved model reproduces the shape of the NFW density profile and its dependence on halo mass and the type of cosmological power spectrum. The NFW profile is also reproduced in studies taking into account the merging mechanism (see Lacey & Cole 1993) in the halo formation scenario (e.g. Salvador-Solé, Solanes & Manrique 1998, Avila-Reese, Firmani & Hernandez 1998). Therefore the numerical and analytical considerations seem to converge on the statement that the density profiles of dark matter haloes are indeed well described by the universal formula proposed by NFW.

The ultimate test of both the analytical and numerical results must come from the observations of density profiles of galaxies and galaxy clusters. Three recent studies of clusters (Carlberg et al. 1997, Adami et al. 1998, van der Marel et al. 1999) claim good agreement between cluster observations and the NFW mass density profile. But for galaxies, the situation is less satisfying. Flores & Primack (1994) show that the NFW profile is incompatible with the rotation curves of spiral galaxies, while Kravtsov et al. (1998) estimate that the inner slope of the density profile of dwarf irregular and LSB galaxies is  $-0.3$  instead of  $-1$ . However, these conclusions were obtained with a number of assumptions and approximations concerning the very unclear issues of biasing, non-sphericity of objects and so on. Nonetheless, it could very well be that in the inner parts of spiral galaxies, a dominant, nearly homogeneous, baryonic core, produced by dissipative physics, could cause a lower inner slope for the dark matter.

The main motivation for this research is to explore analytically the physical properties of objects with NFW density profiles. The aim is to check whether these properties are acceptable from the physical point of view and thus to test the validity of density profiles obtained in cosmological  $N$ -body simulations. Additionally, this paper presents formulas for observable quantities that can be used for comparisons between the theoretical predictions (such as the NFW profile) and observations.

The paper is organized as follows: after a short presentation of the universal formula for the density profile proposed by NFW in Section 2, we describe physical properties of spherical systems following from this density profile. The discussion follows in Section 3.

## 2 PROPERTIES OF THE NFW MODEL

### 2.1 Basic properties

NFW established that the density profiles of dark matter haloes in high resolution cosmological simulations for a wide range of masses and for different initial power spectra of density fluctuations are well fitted by the formula

$$\frac{\rho(r)}{\rho_c^0} = \frac{\delta_{\text{char}}}{(r/r_s)(1+r/r_s)^2} \quad (1)$$

with a single fitting parameter  $\delta_{\text{char}}$ , the characteristic density. The so-called scale radius  $r_s$  is defined by

$$r_s = \frac{r_v}{c}, \quad (2)$$

where  $r_v$  is the virial radius usually defined as the distance from the centre of the halo within which the mean density is  $v$  times the present critical density,  $\rho_c^0$ . The value of the virial overdensity  $v$  is often assumed to be  $v = 178$ , a number predicted by the simplest version of the spherical model for  $\Omega = 1$ . For other values of  $\Omega$  it can be lower by a factor of 2 (Lacey & Cole 1993, Eke, Cole & Frenk 1996). However, according to the improved spherical infall model (Lokas 2000)  $v$  can be as low as 30 even for  $\Omega = 1$ . In the following,  $v$  is kept as a free parameter.

The quantity  $c$  introduced in equation (2) is the *concentration parameter*, which is related to the characteristic density by

$$\delta_{\text{char}} = \frac{v c^3 g(c)}{3}, \quad (3)$$

where

$$g(c) = \frac{1}{\ln(1+c) - c/(1+c)}. \quad (4)$$

The concentration parameter will be used hereafter as the only parameter describing the shape of density profile. From cosmological  $N$ -body simulations (Navarro et al. 1997, Jing 1999, Bullock et al. 1999, Jing & Suto 2000), extended Press-Schechter theory (Navarro et al. 1997, see also Salvador-Solé et al. 1998), and analytical calculations (Lokas 2000), we know that  $c$  depends on the mass of object and the form of the initial power spectrum of density fluctuations. For all initial power spectra, the observed trend is for lower concentration parameter in higher mass objects, with  $4 < c < 22$  in cosmological simulations with CDM initial power spectra and  $c$  up to 90 for the less realistic scale-free power spectra. More precisely, in the  $\Lambda$ CDM cosmology,  $c = 5$  corresponds to the masses of clusters of galaxies, while  $c = 10$  corresponds to the masses of bright galaxies.

It is convenient to express the distance from the centre of the object in units of the virial radius  $r_v$ :

$$s = \frac{r}{r_v} \quad (5)$$

and the density profile of equation (1) then becomes

$$\frac{\rho(s)}{\rho_c^0} = \frac{v c^2 g(c)}{3 s (1+cs)^2}. \quad (6)$$

The mass of the halo is usually defined as the mass within the virial radius:

$$M_v = \frac{4}{3} \pi r_v^3 v \rho_c^0. \quad (7)$$

The distribution of mass in units of the virial mass follows from equation (6):

$$\frac{M(s)}{M_v} = g(c) \left[ \ln(1+cs) - \frac{cs}{1+cs} \right] \quad (8)$$

and we see that it diverges at large  $s$ , which is a disadvantage of the model from a physical point of view.

The gravitational potential associated with the density distribution (6) is

$$\frac{\Phi(s)}{V_v^2} = -g(c) \frac{\ln(1+cs)}{s}, \quad (9)$$

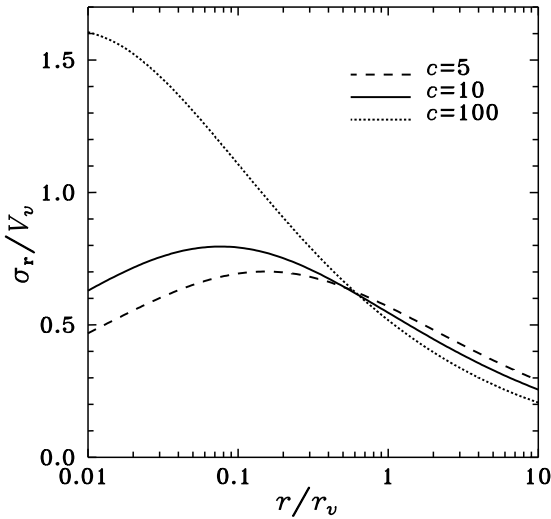


**Figure 1.** Radial velocity dispersion profile (in units of the circular velocity at the virial radius), given by equation (13) for three different values of the concentration parameter  $c$ .

where  $V_v$  is the circular velocity at  $r = r_v$ :

$$V_v^2 = V^2(r_v) = \frac{GM(r_v)}{r_v} = \frac{4}{3} \pi G r_v^2 v \rho_c^0. \quad (10)$$

Hence, from equation (9), the gravitational potential at the centre,  $\Phi(0) = -cg(c)V_v^2$  is finite, in contrast with the potential of the equivalent density profile with an inner slope of  $-1.5$ . Equations (8) and (10) lead to a circular velocity that obeys

$$\frac{V^2(s)}{V_v^2} = \frac{g(c)}{s} \left[ \ln(1+cs) - \frac{cs}{1+cs} \right]. \quad (11)$$

Equations (8), (9) and (11) were first derived by Cole & Lacey (1996).

The radial velocity dispersion  $\sigma_r(r)$  can be obtained by solving the Jeans equation

$$\frac{1}{\rho} \frac{d}{dr} (\rho \sigma_r^2) + 2\beta \frac{\sigma_r^2}{r} = -\frac{d\Phi}{dr}, \quad (12)$$

where  $\beta = 1 - \sigma_\theta^2(r)/\sigma_r^2(r)$  is a measure of the anisotropy in the velocity distribution. In the case of isotropic orbits, which we consider here,  $\sigma_\theta(r) = \sigma_r(r)$  and  $\beta = 0$ . This choice is motivated not only by simplicity, but also by the results of  $N$ -body simulations: Cole & Lacey (1996) and Thomas et al. (1998) show that, in a variety of cosmological models, the ratio  $\sigma_\theta/\sigma_r$  is not far from unity and decreases slowly with distance from the centre to reach  $\simeq 0.85$  at the virial radius.\*

\* However, Huss, Jain & Steinmetz (1999a) find  $\sigma_\theta/\sigma_r \simeq 0.6$  at  $r_v$ .

The solution of equation (12) with the condition of  $\sigma_r \rightarrow 0$  at  $s \rightarrow \infty$  is

$$\begin{aligned} \frac{\sigma_r^2(s)}{V_v^2} &= \frac{1}{2} g(c) s (1+cs)^2 \left\{ c^2 [\pi^2 - \ln(cs)] \right. \\ &\quad - \frac{c}{s} - \frac{c^2}{(1+cs)^2} - \frac{6c^2}{1+cs} \\ &\quad + \left( c^2 + \frac{1}{s^2} - \frac{4c}{s} - \frac{2c^2}{1+cs} \right) \ln(1+cs) \\ &\quad \left. + 3c^2 \ln^2(1+cs) + 6c^2 \text{Li}_2(-cs) \right\}, \end{aligned} \quad (13)$$

where

$$\text{Li}_2(x) = \int_x^0 \frac{\ln(1-t)dt}{t} \simeq x \left[ 1 + 10^{-0.5} (-x)^{0.62/0.7} \right]^{-0.7} \quad (14)$$

is the dilogarithm, and the second equality of equation (14) is accurate to better than 1.5% in the range  $-100 < x < 0$ . Figure 1 shows the radial dependence of the radial velocity dispersion.

## 2.2 The energy distributions

The potential energy associated with the mass distribution of equation (8) is

$$\begin{aligned} W(s) &= -\frac{1}{r_v} \int_0^s \frac{GM(s)}{s} \frac{dM(s)}{ds} ds \\ &= -W_\infty \left( 1 - \frac{1}{(1+cs)^2} - \frac{2\ln(1+cs)}{1+cs} \right), \end{aligned} \quad (15)$$

where

$$W_\infty = -\lim_{s \rightarrow \infty} W(s) = \frac{cg^2(c)}{2} \left( \frac{GM_v^2}{r_v} \right). \quad (16)$$

The kinetic energy takes on a more complicated form:

$$\begin{aligned} T(s) &= 6\pi r_v^3 \int_0^s \rho(s) \sigma_r^2(s) s^2 ds \\ &= \frac{1}{2} W_\infty \left\{ -3 + \frac{3}{1+cs} - 2 \ln(1+cs) \right. \\ &\quad + cs [5 + 3 \ln(1+cs)] - c^2 s^2 [7 + 6 \ln(1+cs)] \\ &\quad \left. + c^3 s^3 [\pi^2 - \ln c - \ln s + \ln(1+cs) \right. \\ &\quad \left. + 3 \ln^2(1+cs) + 6 \text{Li}_2(-cs)] \right\}, \end{aligned} \quad (17)$$

where we have used equation (13) for the radial velocity dispersion.

The results for the potential and kinetic energy (15)-(17) lead to a virial ratio

$$\lim_{s \rightarrow \infty} \frac{2T}{|W|} = 1, \quad (18)$$

for any value of  $c$ , in agreement with the virial theorem. Figure 2 shows the radial variation of the virial ratio. At low radii, the virial ratio is large, especially for low concentration parameters. However, as demonstrated by Figure 3, at the virial radius  $r_v(s=1)$ ,  $2T/|W|$  is still slightly greater than unity. We see that the virial theorem is better satisfied at  $s = 1$  for objects with larger concentration parameters, as

$$\lim_{c \rightarrow \infty} \frac{2T}{|W|}(s=1) = 1. \quad (19)$$

Since objects of smaller mass have larger concentration parameters, they are closer to dynamical equilibrium.

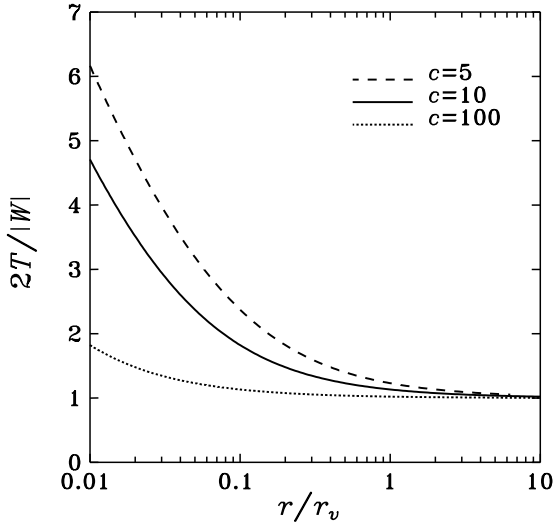


**Figure 2.** The radial dependence of the virial ratio (eqs. [15] and [17]) for three different values of the concentration parameter.

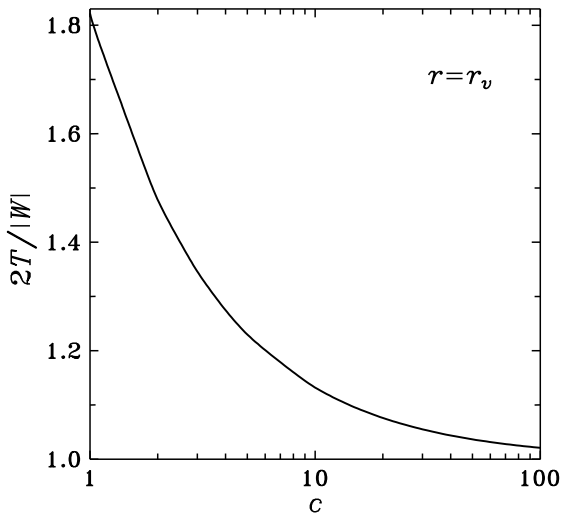


**Figure 3.** Dependence on the concentration parameter of the virial ratio (eqs. [15] and [17]) at the virial radius.

The scalar virial theorem we referred to above is expected to be satisfied for self-gravitating systems in steady state. In more realistic situations the system is never isolated and experiences an external gravitational field; there is also continuous infall of matter. We may conclude from the results above that objects with NFW density profiles and isotropic velocity distributions are close to dynamical equilibrium. However, the virial ratio cannot be used to define the boundary of the virialized object.

### 2.3 Structural parameters

Another useful quantity is the half-mass radius. Unfortunately, the divergence of the mass of the NFW profile forces

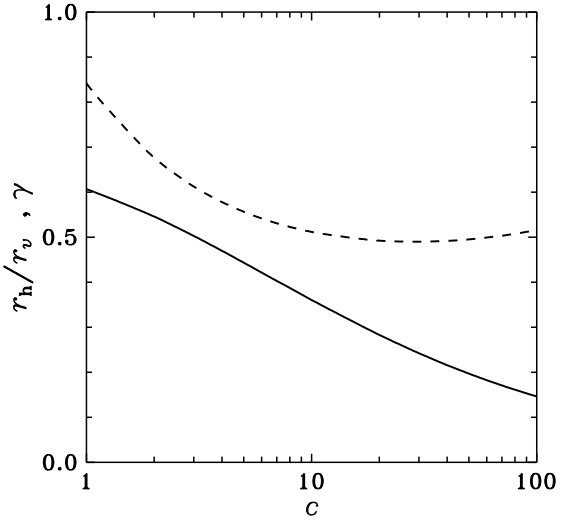


**Figure 4.** Dependence on the concentration parameter of the half-mass radius, scaled to the virial radius (solid curve, see eq. [21]) and  $\gamma$  (eq. [23], dashed curve).

one to define the half-mass radius within a cutoff radius  $r_{\text{cut}}$ . The most natural choice is  $r_{\text{cut}} = r_v$ , since the density distribution is only reliable out to the virial radius. With  $r_{\text{cut}} = r_v$ , the half-mass radius  $r_h$  satisfies the following relation for the mass of dimensionless radius:

$$M\left(\frac{r_h}{r_v}\right) = \frac{M(1)}{2}. \quad (20)$$

Numerical values of  $r_h/r_v$  are easily obtained using equation (8) and over the range  $1 < c < 100$  they can be approximated to better than 2% accuracy by

$$\frac{r_h}{r_v} = 0.6082 - 0.1843 \log c - 0.1011 \log^2 c + 0.03918 \log^3 c. \quad (21)$$

Figure 4 shows how  $r_h/r_v$  decreases with increasing concentration parameter.

It is useful to estimate the concentration  $\gamma$  of a dynamical system, such that

$$3 \langle \sigma^2 \rangle = \gamma \frac{GM}{r_h}, \quad (22)$$

where  $\langle \sigma^2 \rangle$  is the mass weighted mean radial velocity dispersion. As first noted by Spitzer (1969) for polytropes, many realistic density profiles have  $\gamma = 0.4$ . For example, it is easy to show that for the Hernquist (1990) model,  $\gamma = (1 + \sqrt{2})/6 \simeq 0.403$  (Mamon 2000).

Using equation (22) and limiting again the mass to  $r_{\text{cut}} = r_v$ , we define  $\gamma$  with

$$\gamma = \frac{3 r_h \langle \sigma^2 \rangle_{r \leq r_v}}{GM(1)} = 2 \frac{r_h T(1)}{GM^2(1)}, \quad (23)$$

where we made use of

$$T(x) = \frac{3}{2} M(x) \langle \sigma^2 \rangle_{r \leq x r_v}. \quad (24)$$

The values of  $\gamma$  derived from equations (7), (8), (16), (17), (21), and (23) are shown in Figure 4 and yield  $\gamma = 0.56$

for  $c = 5$  and  $\gamma = 0.51$  for  $c = 10$ . Thus the NFW model produces  $\gamma$ s that are higher than the canonical value of 0.4. This may be caused by the ill-defined cutoff radius.

In models with homogeneous cores, the central density, core radius and central velocity dispersion are related through

$$4\pi G\rho(0)r_c^2 = \eta\sigma^2(0), \quad (25)$$

where  $r_c$  is the core radius. King (1966) models have  $\eta = 9$ . In models with cuspy cores, we propose the scaling relation

$$4\pi G\rho(r_s)r_s^2 = \eta\langle\sigma^2\rangle_{r < r_s}, \quad (26)$$

where  $\langle\sigma^2\rangle_{r < r_s}$  is the rms mass-weighted velocity dispersion within  $r \leq r_s$ . Using equations (2), (6) and (7), one has

$$4\pi G\rho(r_s)r_s^2 = \frac{1}{4}cg(c)V_v^2. \quad (27)$$

Then from equation (24) for  $x = 1/c$  one obtains

$$\begin{aligned} \eta &= \frac{3}{2} [4\pi G\rho(r_s)r_s^2] \frac{M(1/c)}{T(1/c)} \\ &= \frac{3(\ln 2 - 1/2)}{\pi^2 - 7 - 8\ln 2 + 6\ln^2 2} \simeq 2.797, \end{aligned} \quad (28)$$

where we have used equations (8), (16) and (17), and the fact that  $\text{Li}_2(-1) = -\pi^2/12$ . Note that  $\eta$  is independent of  $c$ .

#### 2.4 The distribution function

A quantity of great dynamical importance is the distribution function. For a spherical system with an isotropic velocity tensor, the distribution function depends on the phase-space coordinates only through the energy (e.g. Binney & Tremaine 1987), and can be derived through the Eddington (1916) formula (e.g. Binney & Tremaine 1987):

$$f(\mathcal{E}) = \frac{1}{\sqrt{8\pi^2}} \left[ \int_0^{\mathcal{E}} \frac{d^2\rho}{d\Psi^2} \frac{d\Psi}{\sqrt{\mathcal{E}-\Psi}} + \frac{1}{\mathcal{E}^{1/2}} \left( \frac{d\rho}{d\Psi} \right)_{\Psi=0} \right], \quad (29)$$

where  $\mathcal{E}$  and  $\Psi$  are the conventionally defined relative energy and potential; here  $\mathcal{E} = -E$ , where  $E$  is the total energy per unit mass and  $\Psi = -\Phi$ , where  $\Phi$  is given by equation (9).

It is easy to show that, given equations (6) and (9), the second term in brackets in equation (29) is zero. The integration of the first term in brackets in equation (29) is conveniently performed by introducing the dimensionless variables  $\tilde{\Psi} = \Psi/C_1$  and  $\tilde{\rho} = \rho/C_2$ , where  $C_1 = g(c)V_v^2$  and  $C_2 = c^2g(c)M_v/(4\pi r_v^3)$ . Then we may approximate the relation  $s(\Psi)$  needed for the calculation of the derivatives of density with respect to potential in equation (29) by

$$s_{\text{apx}} = -1.75 \frac{1}{\tilde{\Psi}} \ln \left( \frac{\tilde{\Psi}}{c} \right). \quad (30)$$

Figure 5 shows that the residuals of the approximation of equation (30) are better than 16% within the virial radius.

The calculations of the distribution function are usually performed in units such that  $G = M = R_e = 1$  (Binney & Tremaine 1987), where  $M$  is the total mass of the system and  $R_e$  is its effective radius. Since in the case of NFW profile the total mass is infinite a reasonable choice seems to be to put  $M_v = 1$ . The effective radius is not well defined either but can be approximated as  $r_v/2$  (see the next subsection).

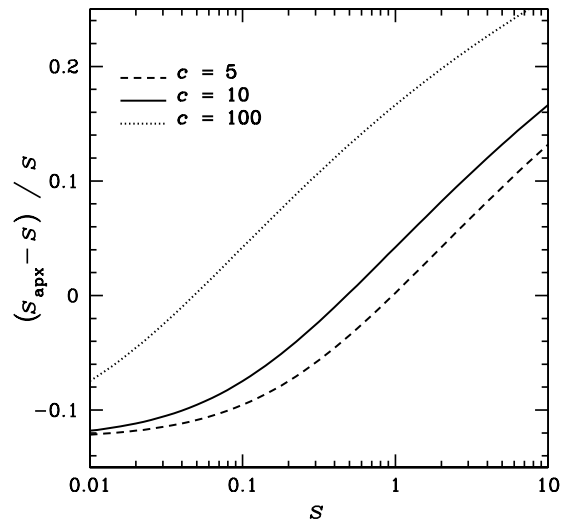


Figure 5. Accuracy of the approximation of equation (30) for three different values of the concentration parameter.

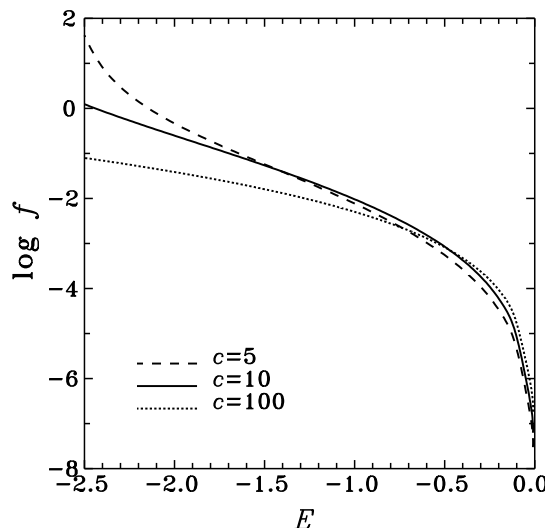
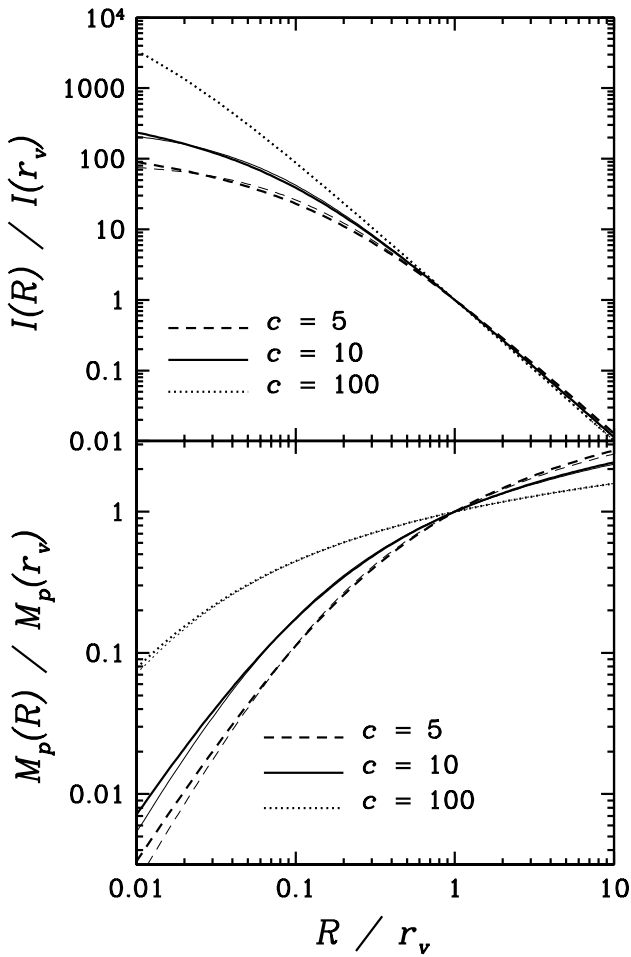


Figure 6. The distribution function (eq. [29]) for three different values of the concentration parameter.

Therefore we choose the units so that  $G = M_v = r_v/2 = 1$  and arrive at the numerical results shown in Figure 6. This choice of normalization is equivalent to measuring  $f$  in units of  $\sqrt{8M_v/(r_v V_v)^3}$  and  $E$  in units of  $V_v^2$ .

Figure 6 proves that the distribution function turns out to be similar to the distribution functions obtained from other density distributions (see e.g. Figure 4-12 in Binney & Tremaine 1987), except that the NFW distribution functions do not display the cutoff at nearly unbound energies characteristic of King (1966) models. The results shown in Figure 6 indicate a proper behaviour of the distribution function (it is nowhere negative). Quantitative comparisons with other models should, however, be made with caution because of



**Figure 7.** Radial profiles of the surface mass density, given by equation (31), (upper panel) and the projected mass, equation (32), (lower panel) for three different values of the concentration parameter. Hubble-Reynolds fits from equation (33) are shown as thin curves ( $R_{\text{HR}}/r_v = 0.119, 0.0640$  and  $0.00743$  for  $c = 5, 10$  and  $100$ , respectively). For  $c = 100$ , the NFW surface mass density is virtually indistinguishable from the best-fitting Hubble-Reynolds law.

the approximation of equation (30) used in the calculations and the aforementioned problem with normalization.

## 2.5 Projected distributions

Of primary importance for comparisons with observations are the projected distributions. The surface mass density of an object is obtained by integrating the density along the line of sight:

$$\Sigma_M(R) = 2 \int_R^\infty \frac{r \rho(r)}{(r^2 - R^2)^{1/2}} dr = \frac{c^2 g(c)}{2\pi} \frac{M_v}{r_v^2} \left[ \frac{1}{c^2 \tilde{R}^2 - 1} - \frac{\cos^{-1}[1/(c\tilde{R})]}{(c^2 \tilde{R}^2 - 1)^{3/2}} \right], \quad (31)$$

where  $R$  is the projected radius and  $\tilde{R} = R/r_v$ . For  $R < r_s$ , equation (31) still holds if complex algebra is used for the numerator and denominator of the second term in parenthe-

ses (or by replacing  $\cos^{-1}$  by  $\cosh^{-1}$  in the numerator and using the absolute value of the term in parentheses in the denominator). An analytical formula equivalent to equation (31) was derived independently by Bartelmann (1996).

The projected mass is then given by

$$M_p(R) = 2\pi \int_0^R R \Sigma_M(R) dR = g(c) M_v \left[ \frac{\cos^{-1}[1/(c\tilde{R})]}{(c^2 \tilde{R}^2 - 1)^{1/2}} + \ln \left( \frac{c\tilde{R}}{2} \right) \right] \quad (32)$$

which is logarithmically divergent at large  $\tilde{R}$ . Again, complex algebra can be used for  $R < r_s$  (or replacement of  $\cos$  by  $\cosh$  in eq. [32] and insertion of absolute values inside the square root term).

Comparisons of the surface mass density to surface brightness observations are usually performed with the assumption of constant mass-to-light ratio  $\Upsilon = \text{const}$ . We then have  $\Sigma_M(R) = \Upsilon I(R)$ , where  $I$  is the surface brightness. The radial profiles of  $I = \Sigma_M/\Upsilon$  and  $M_p$  are shown in Figure 7. Both quantities are normalized to their values at the virial radius. Figure 7 shows that the surface mass density depends weakly on the concentration parameter, especially at larger distances from the centre.

Since the surface mass density (eq. [31]) behaves as  $1/R^2$  at large distances, one may therefore compare it with the Hubble-Reynolds formula (Reynolds 1913), which was the first model used to describe the surface brightness profiles of elliptical galaxies:

$$I_{\text{HR}}(R) = \frac{I_0}{(1 + R/R_{\text{HR}})^2}. \quad (33)$$

$R_{\text{HR}}$  is the characteristic radius of the distribution, where the surface brightness falls to one-quarter of its central value. The thin curves of Figure 7 show that the surface mass density of the NFW model (eq. [31]) is very well fitted by equation (33) and the best-fit values of  $R_{\text{HR}} = R_{\text{HR}}/r_v$  are  $0.119$ ,  $0.0640$  and  $0.00743$  respectively for  $c = 5, 10$  and  $100$ .

The surface brightness profiles of astrophysical objects are often scaled with the *effective radius*, which we denote  $R_e$ , where the projected luminosity is half the total luminosity. Given the divergence of the projected mass, we are forced again to introduce a cut-off at some scale  $R_{\text{cut}} = \tilde{R}_{\text{cut}} r_v$ . We then have

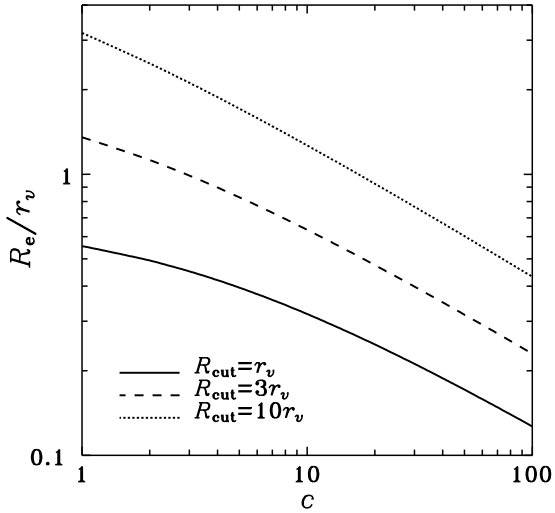
$$M_p(R_e) = M_p(R_{\text{cut}})/2. \quad (34)$$

Figure 8 shows the effective radius, calculated numerically from equations (32) and (34). For  $\tilde{R}_{\text{cut}} = 1$ , a useful approximation, good to better than 2% relative accuracy, is:

$$R_e/r_v = 0.5565 - 0.1941 \log c - 0.0756 \log^2 c + 0.0331 \log^3 c. \quad (35)$$

The prediction for the surface brightness  $I = \Sigma_M/\Upsilon$  with  $\Sigma_M$  given by equation (31) expressed in terms of the effective radius and the corresponding effective brightness  $I_e = I(R_e)$  is shown in the upper panel of Figure 9 for different values of the concentration parameter  $c$ . For comparison, we also show the de Vaucouleurs (1948)  $R^{1/4}$  law describing the observed surface brightness distribution in giant elliptical galaxies:

$$I(R) = I_e \exp[-b(R/R_e)^{1/4}], \quad (36)$$



**Figure 8.** The dependence of the effective radius, defined in equation (34), on the concentration parameter, with various choices of  $\tilde{R}_{\text{cut}}$ .

where  $b = 7.67$ . Clearly, the NFW surface brightness profiles are poorly fitted by the  $R^{1/4}$  law, when using  $R_{\text{cut}} = r_v$  to define the effective radius of the NFW profile.

The lower panel of Figure 9 shows how the results depend on the choice of cut-off for  $c = 10$  and  $\tilde{R}_{\text{cut}} = 3, 3.5, 4, 4.5$ , and 5. At first glance, it seems that the NFW profile is well fitted by the  $R^{1/4}$  law, especially for  $\tilde{R}_{\text{cut}} \simeq 4$ . However, the range of surface mass densities where the fit is excellent is roughly  $10^2$ , and the fit is adequate for a range smaller than  $10^3$ . In contrast, the surface brightness profile of the nearby giant elliptical galaxy NGC 3379 (M 105) follows the  $R^{1/4}$  law in a range of 10 magnitudes (de Vaucouleurs & Capaccioli 1979), i.e. a factor  $10^4$  in intensity.

Moreover, in this galaxy, the  $R^{1/4}$  surface brightness profile (de Vaucouleurs & Capaccioli 1979) extends to  $R_{\text{lim}} = 7.5 R_e = 26.4$  kpc, given a distance of 12.4 Mpc to NGC 3379 (Salaris & Cassisi 1998). Within  $R_{\text{lim}}$ , de Vaucouleurs & Capaccioli (1979) report a blue magnitude, corrected for galactic extinction of  $B = 10.10$ , yielding a total blue luminosity of  $2.2 \times 10^{10} L_\odot$ , hence a blue luminosity density of  $2.8 \times 10^5 L_\odot \text{ kpc}^{-3}$ . Since the mass within  $R_{\text{lim}}$  must be greater than the mass in stars, we infer that within this radius,  $\Upsilon_B > 8$  (the typical mass to blue luminosity ratio for old stellar populations), yielding an over-density of the galaxy, relative to the critical density  $\rho_c$  of  $v > 1.6 \times 10^4 / (H_0/70 \text{ km s}^{-1} \text{ Mpc}^{-1})^2$ . Therefore, since  $v \gg 100$  (the value at  $r_v$ ), we conclude that  $R_{\text{lim}} \ll r_v$ , hence  $R_e \ll r_v/7.5$ . In contrast, with  $\tilde{R}_{\text{cut}} = 1$ , the effective radius of the NFW model ( $c = 10$ ) is  $\simeq 0.3 r_v$  (Figure 8). This discrepancy in  $R_e/r_v$  between NFW and  $R^{1/4}$  law gets even worse if one adopts  $\tilde{R}_{\text{cut}} = 4$ , which provides the best fits of the NFW surface mass density to the  $R^{1/4}$  law: indeed, Figure 8 indicates  $R_e \simeq 0.8 r_v$  for the NFW model.

In summary, the NFW surface mass density profile resembles an  $R^{1/4}$  law in a fairly wide range of radii, but 1) one has to resort to an abnormally large effective radius, very close to the virial radius, and assume that the effective

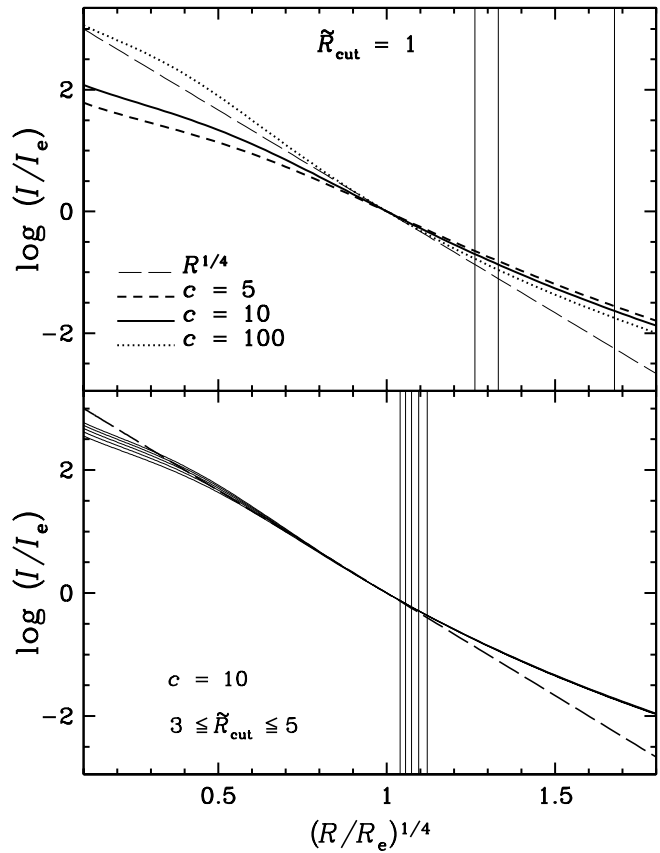


**Figure 9.** *Upper panel:* surface brightness profiles (eq. [31]) for three concentration parameters and  $\tilde{R}_{\text{cut}} = 1$ . *Lower panel:* the dependence of the surface brightness profiles on the cut-off  $\tilde{R}_{\text{cut}}$  for  $c = 10$  and  $\tilde{R}_{\text{cut}} = 3, 3.5, 4, 4.5$ , and 5 (bottom to top curves). In both panels, the  $R^{1/4}$  law (eq. [36]) is shown as long dashed lines. The vertical lines represent the virial radius (for the three concentration parameters in the upper panel and for the 5 values of  $\tilde{R}_{\text{cut}}$  in the lower panel, with  $\tilde{R}_{\text{cut}}$  increasing from right to left).

radius measures half the projected light (or mass) within 4 times the virial radius, and 2) the fit is good in a considerably smaller range of radii than is observed in the nearby giant elliptical NGC 3379.

The generalization of the  $R^{1/4}$  law into an  $R^{1/m}$  law, first proposed by Sérsic (1968), is known to fit the surface brightness profiles of elliptical galaxies within a much larger mass range than the de Vaucouleurs law (Caon, Capaccioli & D'Onofrio 1993). The surface brightness of the Sérsic profile is

$$I(R) = I_e \exp[-b(m) (R/R_e)^{1/m}], \quad (37)$$

where  $b(m)$  is tabulated by Ciotti (1991), who gives the empirical relation  $b(m) \simeq 2m - 0.324$ , good to 0.1% relative accuracy. The de Vaucouleurs law is reproduced for  $m = 4$ , while  $m = 1$  corresponds to an exponential law as in spiral disks.

In Figures 10 and 11, we plot the NFW surface brightness  $I = \Sigma_M / \Upsilon$ , with  $\Sigma_M$  given by equation (31), as a func-

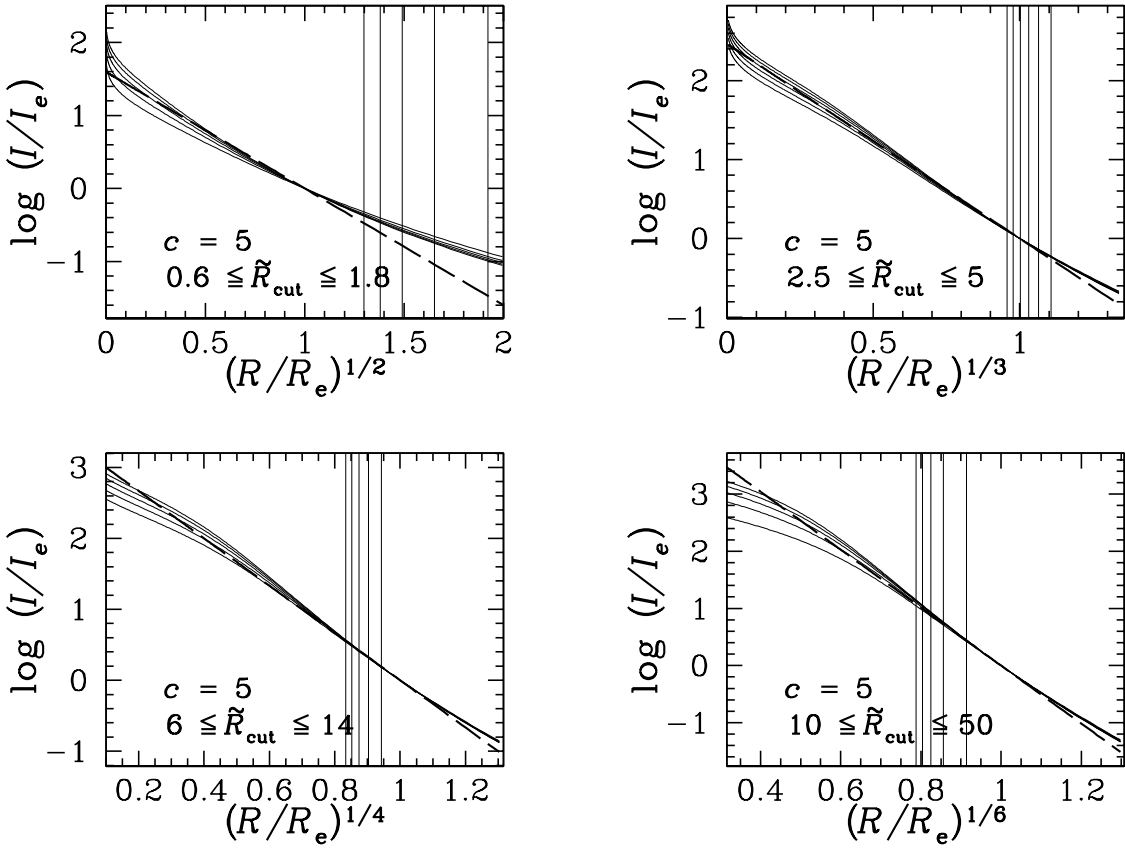


**Figure 10.** Fits of  $c = 5$  projected NFW models (using eq. [31]) to Sérsic models (eq. [37]). The *curves* represent the NFW models (for equally spaced values of  $\tilde{R}_{\text{cut}}$  within the interval indicated in each plot, with  $\tilde{R}_{\text{cut}}$  increasing upwards on the left portion of each plot). The Sérsic law is shown as *long dashed lines*. The *vertical lines* represent the virial radius (with  $\tilde{R}_{\text{cut}}$  increasing from right to left).

tion of  $(R/R_e)^{1/m}$  for various values of the Sérsic parameter  $m$ . The fits are good for all values of  $m$ , within ranges of  $I/I_e$  that increase with increasing  $m$ . Comparison of the plots for different  $m$  shows that the Sérsic models with lower  $m$  generally agree better with the NFW surface brightness for smaller radii, while those with larger  $m$  are in better agreement at larger radii, closer to the virial radius. Overall, for both  $c = 5$  and  $c = 10$ , the NFW profile matches best the  $m = 3$  Sérsic law, over a factor of  $10^3$  in intensity (7.5 magnitudes). While Caon et al. (1993) find similar ranges of agreement between observed profiles and Sérsic laws, this range in intensity is still smaller than the range of  $10^4$  found for NGC 3379 by de Vaucouleurs & Capaccioli (1979). Moreover, while Caon et al. (1993) find that the best fitting Sérsic models for elliptical galaxies have indices spanning a wide range, from  $m = 2$  for faint ellipticals to  $m = 10$  for bright ellipticals, the Sérsic laws that match the NFW models span a much smaller range, roughly  $m = 3 \pm 0.5$ . Moreover, the problem of very high values of  $\tilde{R}_{\text{cut}}$ , hence large  $R_e/r_v$ , remains in the fits of Sérsic profiles to projected NFW models.

Another important projected quantity is the line-of-sight velocity dispersion which for a spherical non-rotating system is (Binney & Mamon 1982)

$$\sigma_{\text{los}}^2(R) = \frac{2}{\Sigma_M(R)} \int_R^\infty \left(1 - \beta \frac{R^2}{r^2}\right) \frac{\rho \sigma_r^2 r}{\sqrt{r^2 - R^2}} dr , \quad (38)$$

where  $\Sigma_M(R)$  is given by equation (31). For isotropic orbits,  $\beta = 0$ , and the radial velocity dispersion  $\sigma_r$  is given by equation (13). For circular orbits,  $\sigma_r = 0$ , and one has

$$\sigma_{\text{los}}^2(R) = \frac{1}{\Sigma_M(R)} \int_R^\infty \left(\frac{R}{r}\right)^2 \frac{\rho V^2 r}{\sqrt{r^2 - R^2}} dr , \quad (39)$$

where  $V$  is the circular velocity given by equations (10) and (11). The upper panel of Figure 12 shows the profiles of line-of-sight velocity dispersion (with isotropic orbits), obtained through numerical integration of equation (38) for different concentration parameters. The lower panel of Figure 12 compares the radial profiles of line-of-sight velocity dispersions obtained for  $c = 10$  for isotropic and circular orbits.

For more distant or intrinsically small galaxies, as well as for groups and clusters, spectroscopic observations are often limited to a single large aperture centred on the object (galaxy, group or cluster). The mean velocity dispersion within an aperture (hereafter, *aperture velocity dispersion*) is

$$\sigma_{\text{ap}}^2(R) = \frac{S^2(R)}{M_p(R)} \quad (40)$$

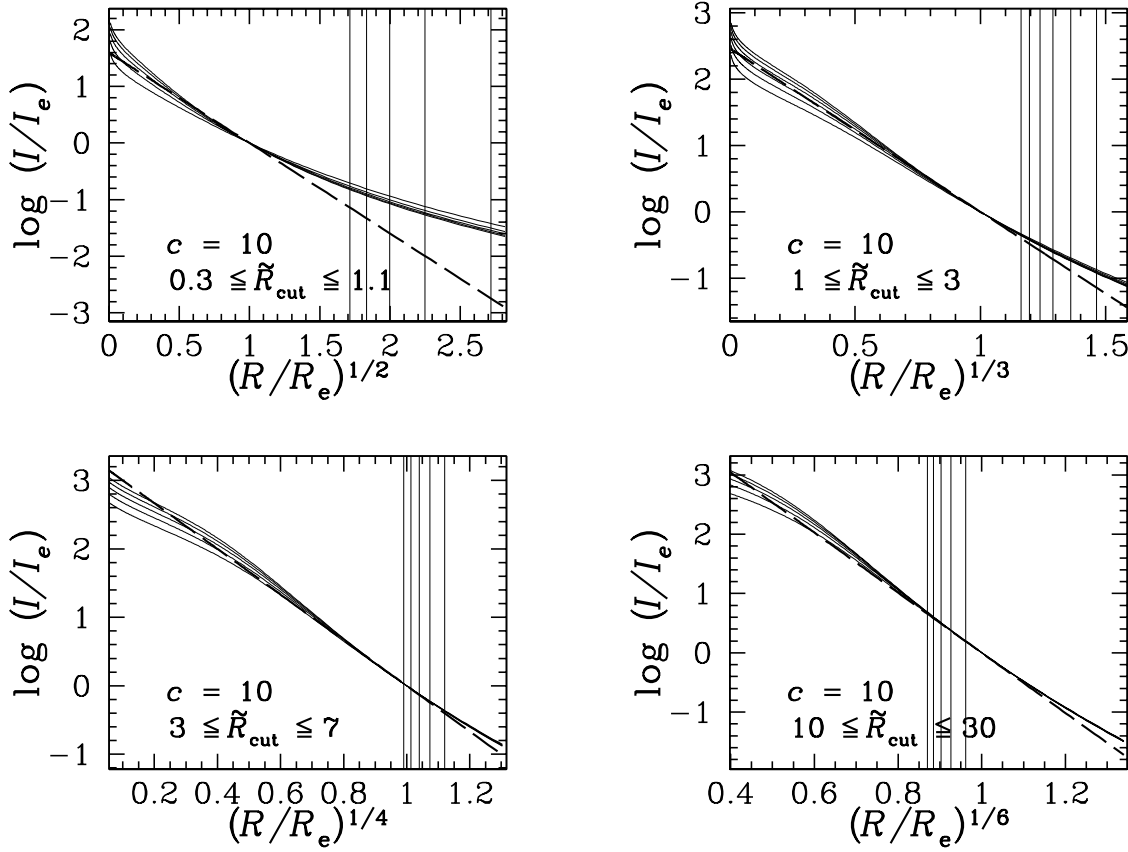


Figure 11. Same as Figure 10, but for  $c = 10$  NFW models.

where

$$S^2(R) = 2\pi \int_0^R \Sigma_M(P) \sigma_{\text{los}}^2(P) P dP. \quad (41)$$

In the above expressions  $R$  is the radius of the aperture,  $\Sigma_M(P)$  is the surface mass distribution, equation (31), and  $M_p(R)$  is the projected mass given by equation (32). We perform the calculation only for isotropic orbits, i.e. with the line-of-sight velocity dispersion  $\sigma_{\text{los}}$  given by equations (38) and (13).

Inserting the expression for  $\sigma_{\text{los}}$  (eq. [38]) into equation (41), we obtain a double integral, which after inversion of the order of integration is reduced to an easily computable single integral:

$$S^2(R) = c^2 g(c) M_v \times \left[ \int_0^\infty \frac{\sigma_r^2(s) s}{(1+cs)^2} ds - \int_{\tilde{R}}^\infty \frac{\sigma_r^2(s) (s^2 - \tilde{R}^2)^{1/2}}{(1+cs)^2} ds \right], \quad (42)$$

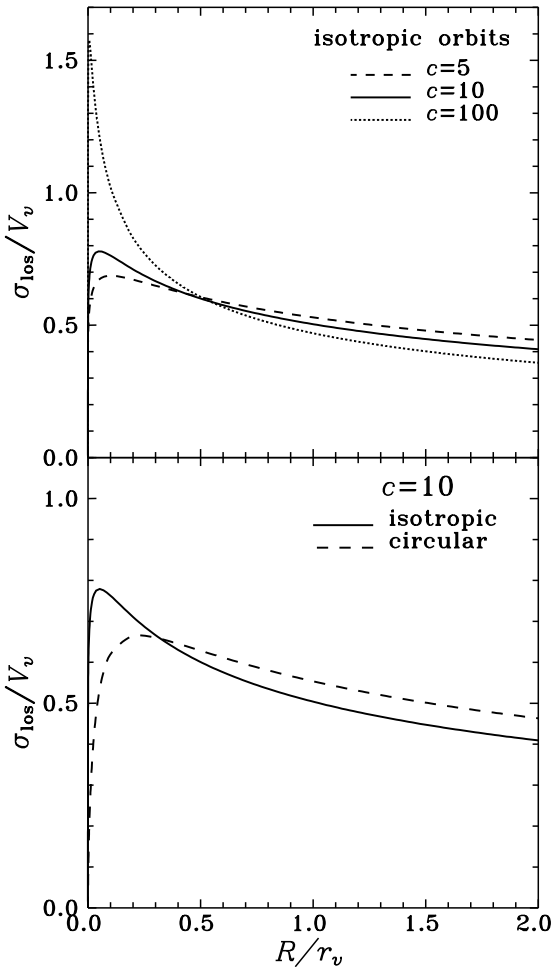
where as before,  $\tilde{R} = R/r_v$  and  $s = r/r_v$ , and  $\sigma_r^2$  is given by equation (13).

Figure 13 displays the radial profiles of aperture velocity dispersion, computed numerically from equation (42). We see that the dependence of the results on the concentration parameter is rather strong and monotonic for a given  $R$ .

### 3 DISCUSSION

The main disadvantage of the NFW model is the logarithmic divergence of its mass (and luminosity for constant mass-to-light ratio). In contrast, the Jaffe (1983) and Hernquist (1990) models converge in mass, and their properties can be expressed in units of their asymptotic mass. For the NFW model, one is restricted to a mass at a physical radius such as the virial radius. This mass divergence also complicates the analysis of surface brightness profiles, which involve the effective radius where the aperture luminosity is half its asymptotic value. However, independently of the radial cut-off introduced to define the effective radius, the projected NFW density profile is consistent with constant mass-to-light ratio, given the observed Sérsic profiles of elliptical galaxies, but only in a limited range of radii, with unusually high values of  $R_e$  and in a smaller interval of Sérsic shape parameters than observed. On the other hand, the Hernquist (1990) model, whose density profile scales as  $r^{-4}$  at large radii, produces better fits to the  $R^{1/4}$  law.

The upper panel of Figure 9 suggests that, for reasonable effective radii, if indeed dark matter follows the NFW profile, the mass-to-light ratio,  $\Upsilon$ , is not constant but increases with radius, not only in the outer regions, as is inferred from the commonly accepted picture of galaxies embedded in more spatially extended dark haloes, but also



**Figure 12.** *Upper panel:* radial dependence of the line-of-sight velocity dispersion for isotropic orbits (eq. [38]) on the projected radius for three values of the concentration parameter. *Lower panel:* comparison of the line-of-sight velocity dispersion profiles for isotropic and circular orbits (eqs. [38] and [39], respectively), calculated with  $c = 10$ .

in the inner regions (with  $\Upsilon$  increasing outwards). This is at odds with the observed kinematics of ellipticals that Bertola et al. (1993) inferred from observations of ionised and neutral gas around specific ellipticals. Moreover, increasing  $\Upsilon$  throughout the galaxy implies radial velocity anisotropy throughout elliptical galaxies, whereas violent relaxation should cause isotropic cores.<sup>†</sup> Thus it appears difficult to reconcile the photometry and kinematics of elliptical galaxies with NFW models.

The results presented in this paper can be directly applied to the analysis of the mass and light distribution in clusters of galaxies. A standard procedure to do it is to mea-

<sup>†</sup> Note that recent, state of the art observations and modelling by Saglia et al. (2000) and Gebhardt et al. (2000) do not strongly constrain the gravitational potentials of elliptical galaxies, although NFW potentials may turn out to be inconsistent with the *current* data.

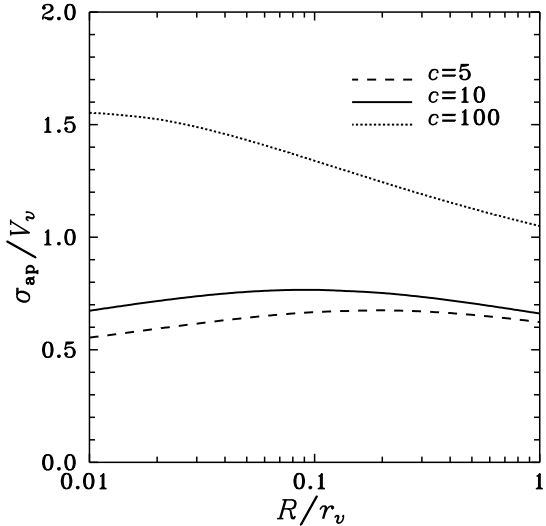


**Figure 13.** Radial profiles of the aperture velocity dispersion (eqs. [40], [42], with [13]) for three concentration parameters.

sure the surface brightness and the light-of-sight velocity dispersion and assuming some form of velocity distribution or mass-to-light ratio calculate the luminosity density and the velocity dispersion by solving the Abel integral equations (31) and (38) and the Jeans equation (Binney & Mamon 1982, Tonry 1983, Solanes & Salvador-Solé 1990, Dejonghe & Merritt 1992). The results of this procedure are uncertain because it involves derivatives of observed quantities which are usually noisy. One also experiences a degeneracy because different models fit the data equally well (Merritt 1987). Instead of solving the Abel equations one can also model the luminosity density and velocity dispersion with simple functions and fit their parameters so that they reproduce their projected counterparts (Carlberg et al. 1997).

Our results are useful for the simpler approach of assuming realistic forms of the density distribution, velocity distribution and mass-to-light ratio. Here we provide the tools for modelling the NFW density profile with an isotropic ( $\beta = 0$ ) velocity distribution and constant mass-to-light ratio ( $\Upsilon = \text{const}$ ), and obtain exact predictions for the surface brightness and the line-of-sight as well as aperture velocity dispersion that can be directly compared to observations. As shown by Carlberg et al. (1997), these assumptions are consistent with their observational data. It would be useful of course to have exact predictions for e.g. other forms of velocity distribution, but unfortunately even for  $\beta = \text{const} \neq 0$  (considered by van der Marel et al. 1999), the analytical solution for velocity dispersion cannot be found and the whole procedure would have to be performed numerically.

## ACKNOWLEDGEMENTS

We thank Daniel Gerbal and Bernard Fort for useful conversations. This work was supported in part by the Polish State Committee for Scientific Research grant No. 2P03D00813.

## REFERENCES

Adami C., Mazure A., Katgert P., Biviano A., 1998, *A&A*, 336, 63

Avila-Reese V., Firmani C., Hernandez X., 1998, *ApJ*, 505, 37

Avila-Reese V., Firmani C., Klypin A., Kravtsov A. V., 1999, *MNRAS*, 310, 527

Bartelmann M., 1996, *A&A*, 313, 697

Bertola F., Pizzella A., Persic M., Salucci P., 1993, *ApJ*, 416, L45

Bertschinger E., 1985, *ApJS*, 58, 39

Binney J., Mamon G. A., 1982, *MNRAS*, 200, 361

Binney J., Tremaine S., 1987, *Galactic Dynamics*. Princeton Univ. Press, Princeton, chap. 4.4.3

Bullock J. S., Kolatt T. S., Sigad Y., Somerville R. S., Kravtsov A. V., Klypin A. A., Primack J. R., Dekel A., 1999, submitted to *MNRAS*, astro-ph/9908159

Caon N., Capaccioli M., D'Onofrio M., 1993, *MNRAS*, 265, 1013

Carlberg R. G. et al., 1997, *ApJ*, L13

Ciotti L., 1991, *A&A*, 249, 99

Cole S., Lacey C., 1996, *MNRAS*, 281, 716

Dejonghe H., Merritt D., 1992, *ApJ*, 391, 531

de Vaucouleurs G., 1948, *Ann. Ap.* 11, 247

de Vaucouleurs G., Capaccioli M., 1979, *ApJS*, 40, 699

Eddington, A. S., 1916, *MNRAS*, 76, 572

Eke V. R., Cole S., Frenk, C.S., 1996, *MNRAS*, 282, 263

Fillmore J. A., Goldreich P., 1984, 281, 1

Flores R. A., Primack J. R., 1994, *ApJ*, 427, L1

Fukushige T., Makino J., 1997, *ApJ*, 477, L9

Gebhardt K. et al., 2000, *AJ*, in press, astro-ph/9912026

Ghigna S., Moore B., Governato F., Lake G., Quinn T., Stadel J., 1999, submitted to *ApJ*, astro-ph/9910166

Gott J. R., 1975, *ApJ*, 201, 296

Gunn J. E., 1977, *ApJ*, 218, 592

Gunn J. E., Gott J. R., 1972, *ApJ*, 176, 1

Hernquist L., 1990, *ApJ*, 356, 359

Hoffman Y., Shaham J., 1985, *ApJ*, 297, 16

Huss A., Jain B., Steinmetz M., 1999a, *MNRAS*, 308, 1011

Huss A., Jain B., Steinmetz M., 1999b, *ApJ*, 517, 64

Jaffe W., 1983, *MNRAS*, 202, 995

Jing Y. P., 1999, submitted to *ApJ*, astro-ph/9901340

Jing Y. P., Suto Y., 2000, *ApJ*, 529, L69

King I. R., 1966, *AJ*, 71, 64

Kravtsov A. V., Klypin A. A., Bullock J. S., Primack J. R., 1998, *ApJ*, 502, 48

Lacey C., Cole S., 1993, *MNRAS*, 262, 627

Lokas E. L., 1999a, in Hammer F. et al., eds, *Proc. XXXIVth Rencontres de Moriond, Building the Galaxies*. Editions Frontières, Gif-sur-Yvette, 423, astro-ph/9909202

Lokas E. L., 1999b, in Mazure A., Le Fèvre O., eds, *Proc. Rencontres Internationales de l'IGRAP, Clustering at High Redshift*. ASP Conference Series, in press, astro-ph/9910182

Lokas E. L., 2000, *MNRAS*, 311, 423

Mamon G. A., 2000, in Combes F. et al., eds, *Proc. XVth IAP Meeting, Dynamics of Galaxies: From the Early Universe to the Present*. ASP Conference Series, 197, 377, astro-ph/9911333

Merritt D., 1987, *ApJ*, 313, 121

Moore B., Governato F., Quinn T., Stadel J., Lake G., 1998, *ApJ*, 499, L5

Navarro J. F., Frenk C. S., White S. D. M., 1995, *MNRAS*, 275, 720

Navarro J. F., Frenk C. S., White S. D. M., 1996, *ApJ*, 462, 563

Navarro J. F., Frenk C. S., White S. D. M., 1997, *ApJ*, 490, 493

Reynolds J. H., 1913, *MNRAS*, 74, 132

Saglia R. P., Kronawitter A., Gerhard O., Bender R., 2000, *AJ*, 119, 153

Salaris M., Cassisi S., 1998, *MNRAS*, 298, 166

Salvador-Solé E., Solanes J. M., Manrique A., 1998, *ApJ*, 499, 542

Sérsic J. L., 1968, *Atlas de Galaxias Australes*, Observatorio Astronomico, Cordoba

Solanes J. M., Salvador-Solé E., 1990, *A&A*, 234, 93

Spitzer L., 1969, *ApJ*, 158, L139

Thomas P. A. et al., 1998, *MNRAS*, 296, 1061

Tonry J. L., 1983, *ApJ*, 266, 58

Tormen G., Bouchet F. R., White S. D. M., 1997, *MNRAS*, 286, 865

van der Marel R. P., Magorrian J., Carlberg R. G., Yee H. K. C., Ellingson E. 1999, submitted to *AJ*, astro-ph/9910494